



Available online at www.sciencedirect.com



ELSEVIER

Nuclear Instruments and Methods in Physics Research A 525 (2004) 465–484

**NUCLEAR
INSTRUMENTS
& METHODS
IN PHYSICS
RESEARCH**
Section A

www.elsevier.com/locate/nima

Test beam analysis of the first CMS drift tube muon chamber

C. Albajar^a, N. Amapane^b, P. Arce^c, C. Autermann^d, M. Bellato^e,
M. Benettoni^f, A. Benvenuti^g, M. Bontenackels^d, J. Caballero^c,
F.R. Cavallo^g, M. Cerrada^c, R. Cirio^b, N. Colino^c, E. Conti^f, B. de la Cruz^c,
F. Dal Corso^f, G.M. Dallavalle^g, C. Fernández^c, J. Fernández de Trocóniz^{a,*},
M.C. Fouz^c, P. García-Abia^c, A. García-Raboso^a, F. Gasparini^f,
U. Gasparini^f, P. Giacomelli^g, F. Gonella^f, M. Gulmini^e,
T. Hebbeker^d, S. Hermann^d, K. Hoepfner^d, I. Jiménez^a, I. Josa^c,
S. Lacaprara^f, S. Marcellini^g, C. Mariotti^b, G. Maron^e, S. Maselli^b,
A.T. Meneguzzo^f, V. Monaco^b, A. Montanari^g, C. Montanari^g,
F. Montecassiano^f, F.L. Navarria^g, F. Odorici^g, M. Passaseo^f,
M. Pegoraro^f, C. Peroni^b, A. Perrotta^g, J. Puerta^c, H. Reithler^d,
A. Romero^b, L. Romero^c, P. Ronchese^f, A. Rossi^g, T. Rovelli^g,
R. Sacchi^b, M. Sowa^d, A. Staiano^b, N. Toniolo^e, E. Torassa^f,
V. Vaniev^b, S. Vanini^f, S. Ventura^f, C. Villanueva^c,
C. Willmott^c, P. Zotto^f, G. Zumerle^f

^a Departamento de Física Teórica C-XI, Universidad Autónoma de Madrid, E28049 Madrid, Spain¹

^b Università di Torino e Sezione dell' INFN, Torino, Italy

^c CIEMAT, División de Física de Partículas, Madrid, Spain¹

^d III. Physikalisches Institut der RWTH, Aachen, Germany

^e Laboratori Nazionali di Legnaro e Sezione dell' INFN, Legnaro, Italy

^f Università di Padova e Sezione dell' INFN, Padova, Italy

^g Università di Bologna e Sezione dell' INFN, Bologna, Italy

Received 8 January 2004; accepted 22 January 2004

Abstract

In October 2001 the first produced CMS Barrel Drift Tube (DT) Muon Chamber was tested at the CERN Gamma Irradiation Facility (GIF) using a muon beam. A Resistive Plate Chamber (RPC) was attached to the top of the DT chamber, and, for the first time, both detectors were operated coupled together. The performance of the DT chamber

*Corresponding author. Tel.: +34-91-397-3881; fax: +34-91-397-3936.

E-mail address: jorge.troconiz@uam.es (J.F. de Trocóniz).

¹ Supported by CICYT.

was studied for several operating conditions, and for gamma rates similar to the ones expected at LHC. In this paper we present the data analysis; the results are considered fully satisfactory.

© 2004 Elsevier B.V. All rights reserved.

PACS: 29.40.Gx

Keywords: LHC; CMS; Muon detector; Drift tubes

1. Introduction

The Barrel Muon Detector of the Compact Muon Solenoid (CMS) experiment is realized by instrumenting four concentric cylindrical stations (MB1, MB2, MB3 and MB4) in the gaps of the return iron yoke. The two inner ones, MB1 and MB2, are equipped with chambers based on a multilayer configuration of Drift Tubes (DT), each chamber having attached two double-gap Resistive Plate Chamber (RPC) planes, one at the top and another one at the bottom. In the case of the MB3 and MB4 drift tube chambers, only one RPC layer is attached. More information about these chambers, Drift Tubes and RPCs, concerning the detection and trigger aspects, can be found in Refs. [1–3]. Results about the performance of the Drift Tubes obtained with prototypes can also be found in Ref. [4] and references therein.

This paper deals no longer with prototypes but with a final chamber, the first one produced, which was tested at the CERN Gamma Irradiation Facility (GIF) for two periods of about 7 days in October 2001. The chamber was a MB2, produced at CIEMAT, consisting of 3 superlayers (2 ϕ and 1 θ) glued together and to a 128-mm thick honeycomb panel. Each superlayer has four layers of drift tubes. The tube cross section is $42 \times 13 \text{ mm}^2$, corresponding to the final version of the drift cell design. All wires inside a superlayer are parallel, with those in even layers staggered by one half cell with respect to those in odd layers. In addition, one RPC (RB2) was attached to the top ϕ superlayer.

The main goal of this test beam was to certify that the performance of a full chamber in an environment with noise conditions similar to the ones expected at the Large Hadron Collider (LHC), satisfies all the CMS requirements. It was

also important to check, and this was the first time it could be done, that the DT and the RPC work properly when coupled together. As reported in Section 7, no problems were found. Results of the analysis of the RPC data alone have been presented elsewhere [5].

A final version of a ROB (ReadOut Board) was connected to 96 channels of the chamber, allowing validation, for the first time, of the performance of this important component of the final readout chamber electronics. The second data taking period was particularly relevant for the test of the ROB since the beam had the 25 ns LHC bunch structure. More details about the ROB and its performance can be found in Ref. [6].

The paper is organized as follows: in Section 2 the experimental setup is introduced. The analysis techniques for pulser and physics runs are presented in Sections 3 and 4, respectively. Section 4 also contains the results on chamber performance at nominal operating conditions. We investigate the evolution of the chamber performance parameters, when the operating conditions and noise levels are changed in Sections 5 and 6, respectively. A possible interference between the DT and RPC chambers is discussed in Section 7. Finally, Section 8 presents the conclusions.

2. Experimental setup

The MB2 chamber was installed inside the GIF experimental zone. In addition to a set of scintillator counters providing the trigger, three delay chambers were used to track the incident muons. The beam covered a chamber area of about $10 \times 10 \text{ cm}^2$; its angular spread was $\sim 2 \text{ mrad}$. Background produced by a ^{137}Cs gamma source, located 4 m upstream of the

chamber, could be switched on and off, and its flux regulated by a system of lead filters. Out of the 17 available attenuation factors 4 were used: 5, 10, 50 and 100, the smallest one providing a background a factor 2 larger than the maximum one to be expected during LHC operation in any of the DT chambers in CMS.

In addition to different background fluxes, data were taken with different conditions of voltage settings, discriminator thresholds, and the RPC HV switched on and off. We used special runs to measure noise (beam off), and test pulse runs for calibration purposes. Most of the time the chamber was placed perpendicular to the beam, with superlayer ϕ_1 in front, followed by the honeycomb panel, superlayer θ , and superlayer ϕ_2 . No special support allowing translations and rotations was available, but the chamber was moved twice in order to have three different regions being hit by the incident muons. In total ~ 200 runs, each one having typically 100,000 events, were taken.

During the first test beam period, P2B, the muon beam was non-structured with an intensity of about 1200 triggers/s. During the second period, P2C, the beam had a 25 ns structure and the trigger rate was 5 kHz.

Multi-hit CAEN TDCs were used for the readout of the discriminated signals coming from the chamber front end electronics. Hits were recorded in a window 4 μ s wide started by the trigger signal. One TDC count corresponded to 25/32 ns ~ 0.78 ns. The results reported in this paper were obtained from the analysis of the data taken with these commercial TDCs. But, in addition, one ROB designed at CIEMAT and equipped with 4 high-performance TDC (HPTDC) chips [7] was also connected part of the time to 96 chamber channels as previously mentioned. The ROB was connected through a set of purpose dedicated boards and a VME interface to a PC for HPTDC programming and monitoring. Control of the readout system, data decodification and spill management was done by software. Data taken with the ROB were analyzed and all results concerning single wire efficiencies, meantime values, hit position resolutions, and drift velocities, were fully consistent with the corresponding ones reported in Section 4.

3. Pulser runs

At the debugging stage, and previously to every physics run, pulser runs were recorded. Test pulses were produced by a pulse generator, split into two similar input pulses by a splitter box, and injected at the electronics front-end. One of the inputs fed wires in layers #1 and #3, and the other layers #2 and #4. The splitter box can introduce a relative delay between the two output pulses, useful for trigger electronics test purposes.

Relative T_0 's were calculated from the leading edge arrival time of the measured pulses. Fig. 1 shows the output time distribution for a typical channel in a typical pulser run (Run 621). The test pulse time resolution is in the range 0.4–0.6 TDC counts, with all the entries in essentially two TDC bins. Fig. 2 shows the average output time as a function of the channel number. These numbers were used in the offline analysis for relative T_0 subtraction.

4. Physics runs

The chamber nominal conditions in physics runs were $V_{\text{wire}} = 3.6$ kV, $V_{\text{strip}} = 1.8$ kV, $V_{\text{cath}} = -1.2$ kV, and a discriminator threshold of

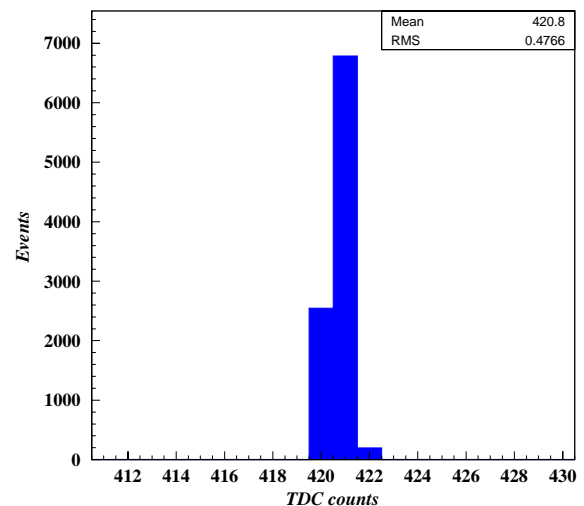


Fig. 1. Output time distribution for a typical channel in pulser Run 621.

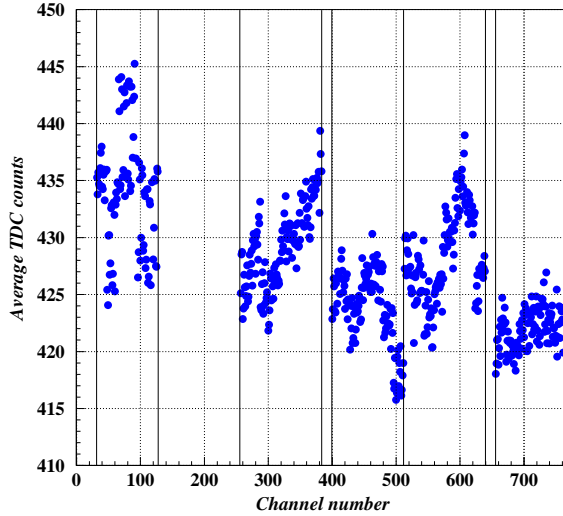


Fig. 2. The average output time as a function of the channel number in pulser Run 621. The vertical lines limit the cabled regions.

15 mV. The typical beam spread covered 4 drift cells in the ϕ superlayers (6 cells in the θ superlayer), corresponding to a total of 16 (24) TDC channels. The proportion of noise hits, dominated by beam-induced backgrounds, was smaller than 10^{-3} .

In this section, we discuss in detail the calibration and analysis procedures. For illustration purposes we use a typical run with 10^6 events (Run 624).

4.1. Calibration and alignment

Hit data must first be corrected for relative and global T_0 . The relative T_0 subtraction method has been described in the previous section. Global T_0 's were equalized looking at the leading edge of the signal time-box using the derivative method. Fig. 3 shows a typical time-box distribution at nominal chamber conditions. Six global T_0 adjustments were calculated, one for the odd (even) layers in each one of the three superlayers. As the input test pulses are different, one has to allow for a possible time shift. In fact, a shift larger than 1 ns was observed for the θ superlayer.

Fig. 4 shows the derivative of the time-box distribution. Fig. 5 shows the derivative in the

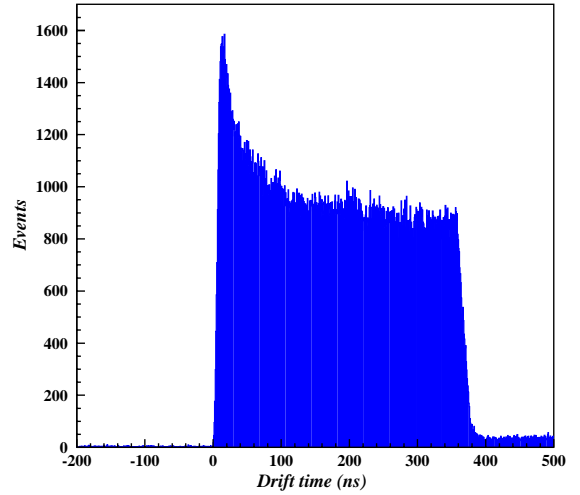


Fig. 3. Typical drift time-box distribution after relative T_0 correction.

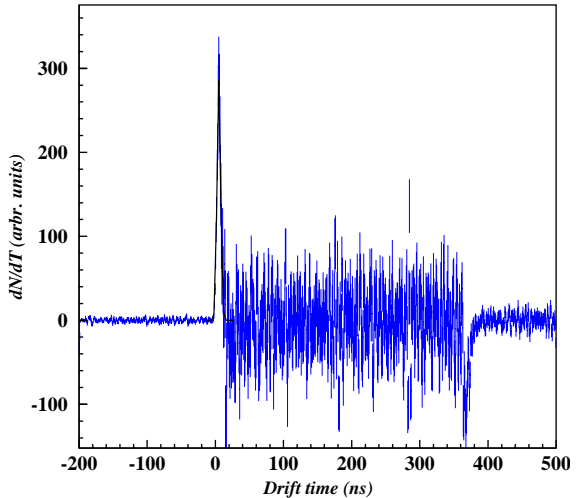


Fig. 4. Derivative of the drift time distribution (arbitrary units).

leading edge region, where a Gaussian fit has been performed. A sigma of 2.68 ± 0.05 ns is obtained. Gaussian widths were in the range 2.4–2.7 ns for the ϕ superlayers (2.9–3.0 ns for the θ superlayer). The T_0 is defined as the Gaussian mean value minus 5 ns. This corresponds to two average sigmas in the negative side of the Gaussian. We preferred to use an average sigma instead of every individual sigma to be less sensitive to the statistical fluctuations of each fit.

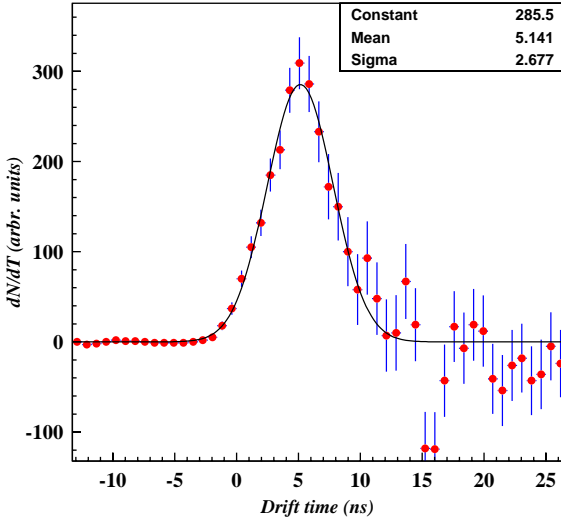


Fig. 5. Detail of the derivative distribution in the leading edge region. The parameters of a Gaussian fit are given.

Hits in every superlayer were fitted to a straight segment by minimizing the χ^2 . All possible fits with at least three hits were studied. No χ^2 cut was attempted at this stage in order to avoid any bias on data selection. To maximize the hit finding efficiency a fit with 4 hits was always preferred to a fit with three hits. For the same number of hits, the fit with the best χ^2 was chosen. In the following analysis only the best fit in every superlayer was considered. In the majority of the cases the presence of several fits was the result of the coincidence of several beam muons traversing the chamber (see Section 6.2). Fig. 6 shows the χ^2 distribution for segments with 4 hits in superlayer ϕ_1 . Units are mm^2 .

Drift velocities were estimated using the meantime method. The meantime (MT_j) is

²The standard χ^2 is defined as the sum of the squared residuals divided by the resolution squared, therefore it is a dimensionless quantity. In this paper we call χ^2 only to the numerator (therefore with dimensions of length squared). The reason to do this is that the denominator, the resolution squared, is a result of the analysis itself and it is not known a priori. On the other hand, in this analysis the resolution is assumed to be the same for all events. Therefore the denominator is just a constant, and, since the χ^2 is only used for minimization and cutting purposes, it is equivalent to use the standard χ^2 or a quantity proportional to it.

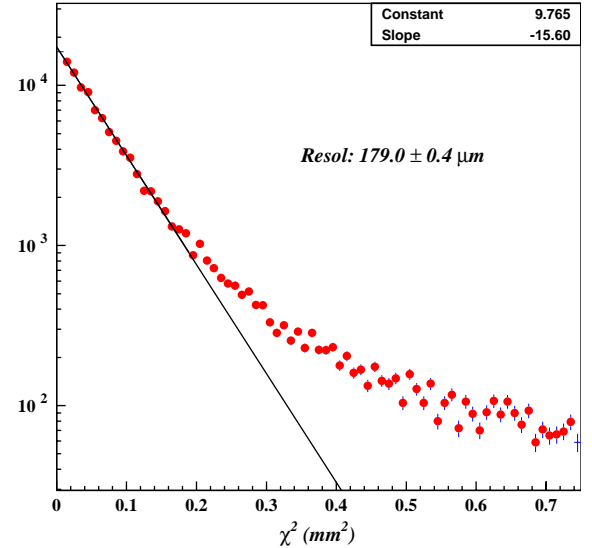


Fig. 6. The χ^2 distribution for 4-hit segments in superlayer ϕ_1 (Run 624). Units are mm^2 . The parameters of an exponential fit to the region $\chi^2 < 0.2 \text{ mm}^2$ are given.

defined as

$$MT_j = \frac{1}{2}[T(j) + T(j+2) + 2T(j+1)]$$

where $T(j)$, $T(j+1)$, and $T(j+2)$ are the drift times measured in three successive layers (j , $j+1$, and $j+2$), and layer ($j+1$) is staggered by half a cell with respect to the other two. The central layer in MT1 (MT2) is #2 (resp., #3).

The histogram in Fig. 7 shows the meantime (MT1) distribution for 4-hit segments in superlayer ϕ_1 . The meantime distribution peaks at the maximal drift time. The tail on the left of the distributions is produced when one or more hits in the fit were produced by delta-rays. Considering only 4-hit segments with $\chi^2 < 0.3 \text{ mm}^2$ eliminates the tail, without disturbing its Gaussian core (points in Fig. 7).

Fig. 8 shows the four meantime distributions, after relative and global T_0 adjustment, for 4-hit segments in superlayer ϕ_1 with $\chi^2 < 0.3 \text{ mm}^2$. L(left) and R(right) denote the segment relative position with respect to the wire in layer #1.

The meantime distributions in Fig. 8 were fitted to a Gaussian shape. Taking into account the maximal drift time and the cell maximal drift distance (21 mm) the drift velocity is measured. In

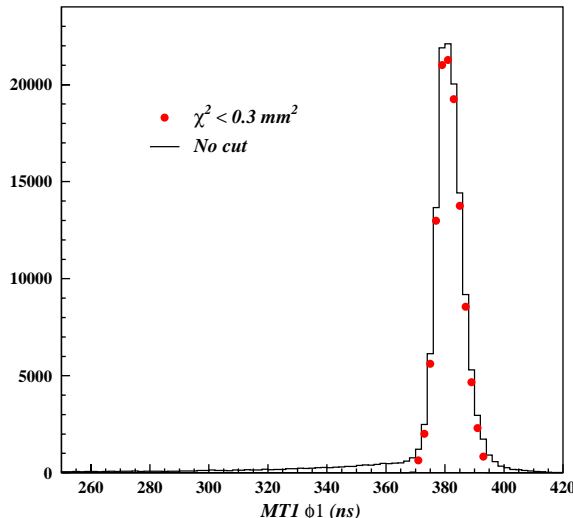


Fig. 7. Meantime (MT1) distribution for 4-hit segments in superlayer ϕ_1 (Run 624). The histogram is for all segments, the points for the subset satisfying $\chi^2 < 0.3 \text{ mm}^2$.

Fig. 8, the mean values of the left and the right Gaussian fits are shifted in opposite directions due to wire position misalignment ($\pm 0.2 \text{ ns}$ for MT1, $\pm 1.0 \text{ ns}$ for MT2). In contrast, the average of the two mean values is insensitive to any misalignment. This can be tested by comparing the average of MT1s to the average of MT2s: in Fig. 8 they agree at the 0.1 ns level. The maximal drift time was thus estimated using the average of the four Gaussian mean values.

The meantime fit mean values and corresponding drift velocities for the three superlayers in Run 624 are summarized in Table 1.

The statistical error in the drift velocity is very small. Systematic errors were estimated by moving around the global T_0 by 1 ns. It is important to note that the drift velocity values depend on the adopted T_0 determination. Without an external position reference all the fits satisfying the relation

$$2\Delta T_0 v_d - T_{\max} \Delta v_d = 0$$

are equivalently good (neglecting quadratic corrections). This formula means that a change in the drift velocity can be perfectly absorbed by a T_0 redefinition, without paying a price in the χ^2 . From the formula, the systematic error on the drift velocity is $0.3 \text{ } \mu\text{m/ns}$.

Once the drift velocities are measured, and since the precision to determine the drift velocity given a T_0 , is better than the precision from the T_0 itself, one can choose instead to fix the drift velocities to a given value inside the systematic window. It is expected that the calibration procedure will be better defined, and the measurement of all other relevant quantities much less sensitive to the statistical fluctuations in the T_0 determination. This is particularly important since the main results in this paper stem from the comparison of the parameters measured in several runs taken under different conditions.

Consequently, the drift velocities were fixed at $55 \text{ } \mu\text{m/ns}$ and the segments re-fitted. Comparing to the drift velocity values in Table 1, all the T_0 's had to be adjusted by a fraction of one resolution sigma.

After T_0 and drift velocity determination, one can use the residual distributions to align the position of the wires. Fig. 9 shows the residual distributions for 4-hit segments in superlayer ϕ_1 . The mean values obtained after fitting a Gaussian shape are then used to calculate the actual wire position displacements.

Missing an external reference the four residuals are not independent, because two degrees of freedom have been absorbed by the fit parameters. These two degrees of freedom correspond physically to an overall translation and rotation offset of the chamber with respect to the beam. Since we are interested only in the relative alignment, one of the displacements can be defined as zero (say the one of layer #1). But to fix the problem one needs another hypothesis. For the case of one superlayer (θ) we adopted the minimal misalignment hypothesis corresponding to the minimal sum of the misalignments squared. In the case of two parallel superlayers one degree of freedom can be fixed imposing that the average slopes in both superlayers coincide. But beyond this, one has to impose again a combined minimal misalignment condition. We note that before imposing a common average slope, the values in the ϕ_1 and ϕ_2 superlayers differ by 4.0 mrad. This number represents well the size of the expected systematic slope shifts before fine wire alignment at CMS. We will see later that this size is comparable to the

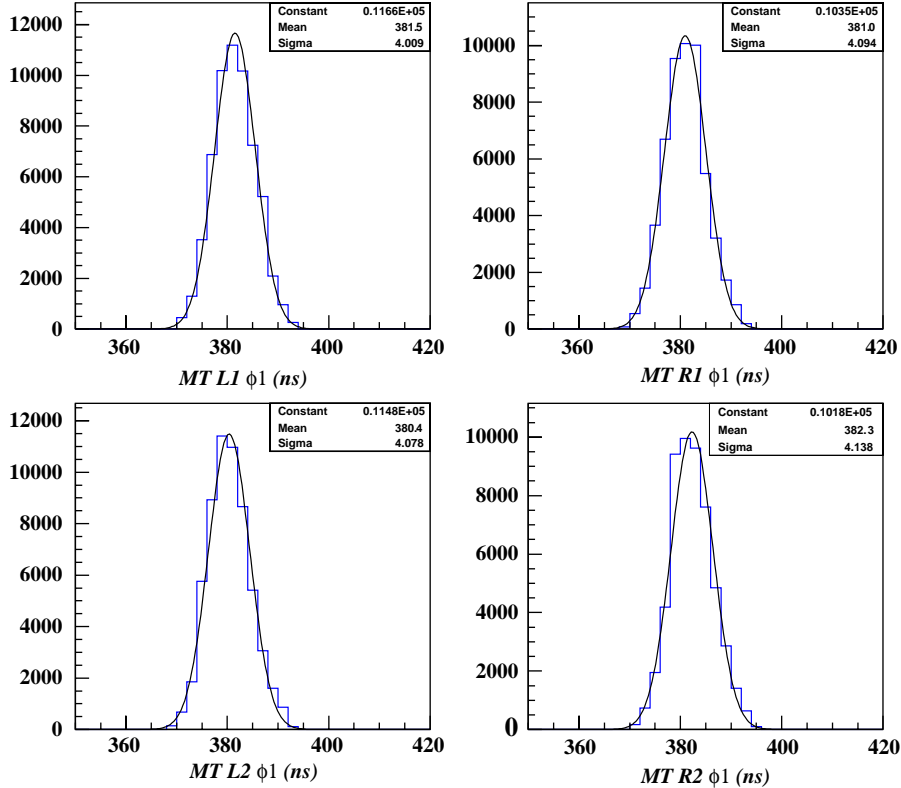


Fig. 8. Meantime distributions, after relative and global T_0 adjustment, for 4-hit segments with $\chi^2 < 0.3 \text{ mm}^2$ in superlayer ϕ_1 (Run 624). The central layer in MT1 (MT2) is #2 (resp., #3). L and R denote the segment relative position with respect to the wire in layer #1. The parameters of the corresponding Gaussian fits are given.

Table 1

Summary of the meantime Gaussian mean values (ns), after T_0 adjustment, and corresponding drift velocities ($\mu\text{m}/\text{ns}$) for the three superlayers in Run 624

	SL θ	SL ϕ_1	SL ϕ_2
MTL1 (± 0.02)	377.8	381.5	380.3
MTR1	383.2	381.0	381.0
MTL2	378.2	380.4	379.2
MTR2	382.5	382.3	381.8
Average MT	380.4	381.3	380.6
$\Delta MT1$	± 2.7	± 0.2	± 0.4
$\Delta MT2$	± 2.1	± 1.0	± 1.3
Drift velocity (± 0.3)	55.21	55.07	55.18

Errors appear in brackets. The numbers ΔMTi are differences from the average MT value.

intrinsic single superlayer angular resolution, and much larger than the double superlayer combined angular resolution. We finally mention that in the case of two ϕ superlayers, all wire displacements are fixed if the shift between the two superlayers (nominally 42 mm) is known.

The residual fit mean values, and corresponding wire position shifts in Run 624 are summarized for the three superlayers in Table 2.

Since the wire position shifts are just of geometrical nature, a cross-check of the calibration and alignment procedure is provided by the stability of the values. Fig. 10 shows the wire alignment parameters calculated for several different runs (parameterized using the corresponding

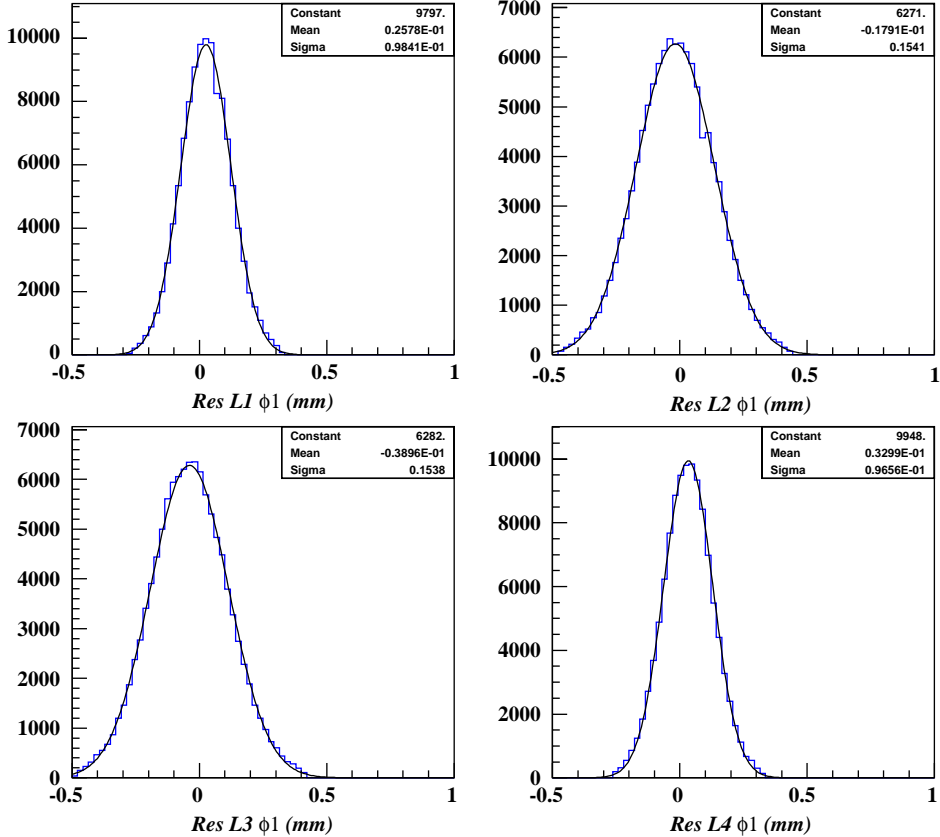


Fig. 9. Residual distributions, after T_0 and drift velocity calibration, for 4-hit ϕ_1 -segments with $\chi^2 < 0.3 \text{ mm}^2$ (Run 624). The parameters of the corresponding Gaussian fits are given.

Table 2

Summary of the residual Gaussian mean values (μm), after T_0 and drift velocity calibration, and corresponding wire misalignments Δx_i (μm) for the three superlayers in Run 624. Errors appear in brackets

	SL θ	SL ϕ_1	SL ϕ_2
Residual layer #1 (± 0.3)	-39.3	25.8	15.4
Residual layer #2	85.8	-17.9	1.2
Residual layer #3	-54.5	-39.0	-47.6
Residual layer #4	8.4	33.0	32.0
Δx_2	108.3	-18.0	-22.2
Δx_3	-48.3	-16.2	-80.1
Δx_4	-3.9	85.2	-7.6

wire voltage value), at two positions in the chamber. The same values, within a few microns, are consistently found.

4.2. Stand-alone parameter determination

After calibration and alignment, we are ready to measure the most important chamber performance parameters: linearity, resolutions, and efficiencies.

A good final check of the calibration and alignment procedure is that the χ^2 distribution of the fitted segments should look like a χ^2 distribution. Particularly interesting is the one corresponding to 4-hit segments shown in Fig. 6, that should be an exponential for the events where the 4 hits are good (Gaussian statistics). Deviations from the exponential shape are interpreted as fits where (at least) one of the hits was originated by a delta-ray. We performed an exponential fit of the data points in Fig. 6 with $\chi^2 < 0.2 \text{ mm}^2$. The parameters of the fit are given in the figure. From the slope a hit position resolution of $179.0 \pm 0.4 \mu\text{m}$ is deduced,

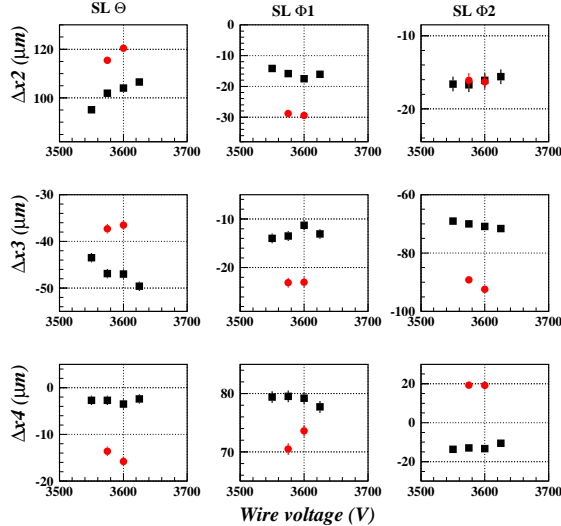


Fig. 10. Wire alignment stability for several runs (parameterized using the corresponding wire voltage value), at two different positions in the chamber (squares and dots).

implying that the cut $\chi^2 < 0.3 \text{ mm}^2$ is at the 3-sigma level. Comparing the integral of the exponential curve to the measured number of events, the power of this cut to discriminate 4-good-hit segments from delta-ray contaminated ones can be quantified. More than 90% of the 4-good-hit segments satisfy the cut, yet the delta-ray contamination is kept at a few percent level.

After calibration and alignment have been applied, the four meantime distributions for 4-hit segments with $\chi^2 < 0.3 \text{ mm}^2$ in superlayer ϕ_1 have been recomputed, and compared to the ones in Fig. 8. We find that the shifts L–R are now $\pm 0.1 \text{ ns}$. Both averaged mean values virtually coincide and correspond to the fixed drift velocity of $55 \mu\text{m}/\text{ns}$. The four Gaussian sigmas are proportional to the hit position resolution. The values for the three superlayers are summarized in Table 3.

Similarly, we can compare the new residual distributions in superlayer ϕ_1 to the ones in Fig. 9. The Gaussian offsets are now within $\pm 10 \mu\text{m}$. Again, the four Gaussian sigmas are proportional to the hit position resolution. The values for the three superlayers appear also in Table 3. Agree-

Table 3

Summary of hit position resolution estimators (μm) and cell efficiencies (%), after T_0 , drift velocity, and wire position adjustments, for the three superlayers in Run 624

	SL θ	SL ϕ_1	SL ϕ_2
MTL1	186.8 ± 0.4	178.3 ± 0.4	181.5 ± 0.4
MTR1	177.5 ± 0.4	184.1 ± 0.4	186.4 ± 0.4
MTL2	186.5 ± 0.4	185.0 ± 0.4	185.0 ± 0.4
MTR2	183.6 ± 0.4	185.0 ± 0.4	181.9 ± 0.4
Residual layer #1	186.7 ± 0.4	178.4 ± 0.4	175.8 ± 0.4
Residual layer #2	188.8 ± 0.5	180.1 ± 0.5	183.9 ± 0.5
Residual layer #3	190.4 ± 0.5	184.4 ± 0.5	178.3 ± 0.5
Residual layer #4	188.2 ± 0.4	179.3 ± 0.4	177.8 ± 0.4
Efficiency	99.92 ± 0.01	99.97 ± 0.01	99.97 ± 0.01

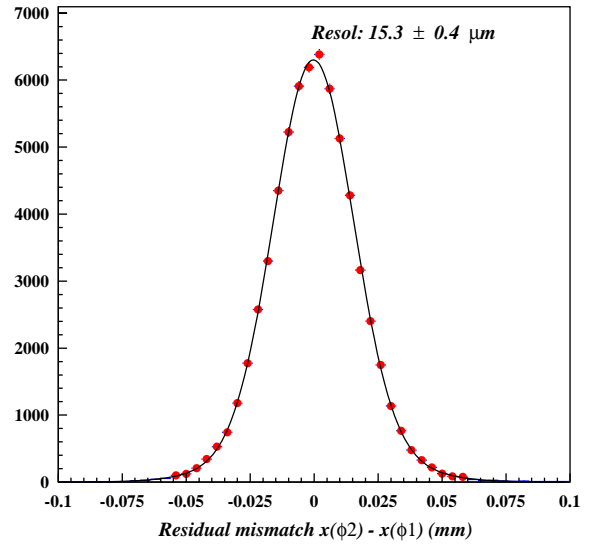


Fig. 11. Distribution of the residual mismatch between positions at superlayers ϕ_1 and ϕ_2 , using the slope of a combined fit to the hits in both superlayers (Run 624).

ment among all the different resolution estimators is satisfactory.

Once the basic hit position resolution is known, all other relevant resolutions can be derived, and compared to their experimental values. For instance, Fig. 11 shows the distribution of the residual mismatch between positions at superlayers ϕ_1 and ϕ_2 , using the slope of a combined fit to the hits in both superlayers. Segments must be

4-hit and have $\chi^2 < 0.3 \text{ mm}^2$ in both superlayers. A resolution of $15.3 \pm 0.4 \mu\text{m}$ is obtained. For a hit position resolution of $180 \mu\text{m}$, the expected extrapolation resolution is $15.5 \mu\text{m}$.

The single hit detection efficiency is calculated from the ratio of the number of 3-hit segments to the number of 4-hit segments. No χ^2 cut is implemented here, as the delta-ray hits also are considered to add to the hit efficiency. There are two main reasons that make a cell inefficient. The first one is geometrical, when the muon traversed the I-beam walls separating a drift cell from the next. The second is the genuine detection inefficiency when the muon traversed the detection region.

For perpendicularly incident muons, the cell wall effect ideally means that two hits are lost and no fit is found. However, sometimes a fit is found after all, contaminating the genuine efficiency calculation. This typically happens when a third hit, originated from a delta-ray, is incorporated into the fit. The effect of this third hit is to pull the fit position away from the wall, simultaneously deteriorating the χ^2 value. The two samples can therefore be separated attending to the χ^2 correlation for 3-hit events versus the internal cell position, as illustrated in Fig. 12 where the previous pattern is obvious. For the accumulation of events with internal positions close to 0 and 21 mm, the inefficiency is attributed to the cell wall effect. For the central events the inefficiency is genuine. The two lines in Fig. 12 are used to separate both regions. The genuine cell efficiency values obtained in Run 624 for the three superlayers are shown in Table 3.

4.3. Parameter determination using an external reference

In order to provide an external reference for the beam, three delay chambers were used. Chambers #1 and #2 were 6700 and 4700 mm upstream, respectively. Chamber #3 was 2300 mm downstream, and behind an iron block $\sim 1 \text{ m}$ thick. The separation between Chambers #1 and #2 was measured to be 2000 mm at GIF.

No calibration run of the chambers at GIF was attempted. We use the data instead. In case of

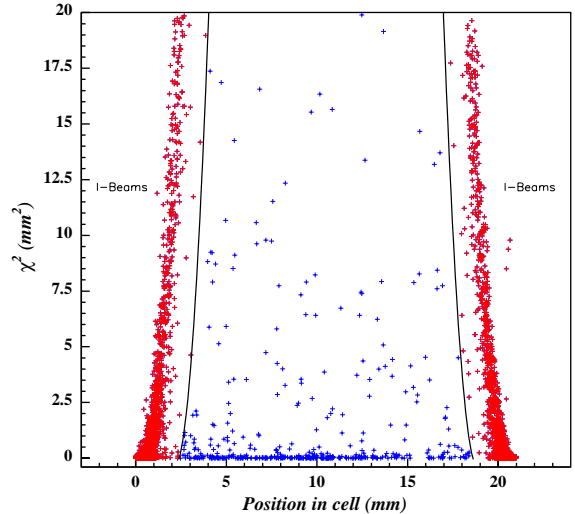


Fig. 12. χ^2 versus internal cell position for 3-hit segments in superlayer ϕ_1 (Run 624).

several hits, correlation of the various hits showed that the first one in time has to be used. Delay chamber T_0 's are relatively less important as they only shift the average beam position and angle. The slope (assumed to be the same for the three chambers), relative positions, and resolutions were estimated using the separation between chambers #1 and #2 to set the scale in the axial direction, and the DT cell size to set the scale in the transverse direction. Fitting events with one good hit in every chamber to a straight line, the minimum χ^2 corresponded to a slope of 0.146 mm/ns and a hit position resolution of $930 \mu\text{m}$ for Chambers #1 and #2. For Chamber #3 after adding the effect of multiple scattering, the resolution deteriorates to $\sim 1.3 \text{ mm}$. Combining the information of the three delay chambers, the expected extrapolated position resolution on the face of the DT chamber is $\sim 1 \text{ mm}$ (one order of magnitude worse than the DT superlayer position resolution). In contrast, the expected angular resolution is $\sim 0.2 \text{ mrad}$, much better even than the combined $\phi_1-\phi_2$ angular resolution.

In this section we select muons measured with both the DT chamber, and with the delay chambers in Run 624. Segments in the DT chamber are required to be 4-hit and have $\chi^2 < 0.3 \text{ mm}^2$ in every relevant superlayer. For

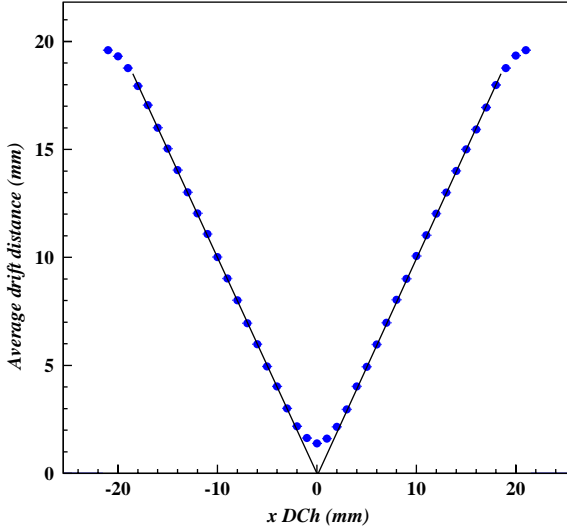


Fig. 13. The average measured drift distance in superlayer ϕ_1 , as a function of the internal cell position obtained with the delay chambers (Run 624). The straight lines have slopes ± 1 .

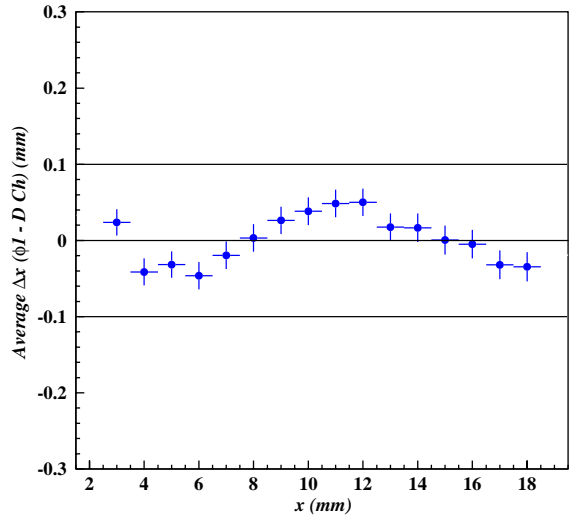


Fig. 14. Deviations from linearity in the previous plot, as a function of the cell internal position obtained with the delay chambers.

the delay chambers we require that the interpolation of Chambers #1 and #3 at the position of Chamber #2 agrees with the actual measurement at Chamber #2 within 3.6 mm (3 sigmas).

We first investigate the linearity of the relation distance from the wire versus drift time. Fig. 13 shows the average measured drift distance in superlayer ϕ_1 , as a function of the internal cell position obtained with the delay chambers. The drift distance is the product of the measured drift time times the drift velocity (fixed during calibration at 55 $\mu\text{m/ns}$). The straight lines have slopes ± 1 . The agreement is good in the region $2.5 \text{ mm} < |x| < 18.5 \text{ mm}$. Distortions around $x = 0$ and $\pm 21 \text{ mm}$ are expected due to the vicinity of the wire or I-beam walls, together with the poor delay chamber extrapolation resolution. In Fig. 14 the deviations from linearity in the previous plot as a function of the cell internal position are observed in detail. All deviations are well within $\pm 100 \mu\text{m}$.

We now turn to the measurement of the muon position and angle resolutions. Figs. 15 and 16 compare the measured horizontal angular and position beam profiles, respectively. The histograms were obtained using a combined fit to the hits in superlayers ϕ_1 and ϕ_2 . The dots were

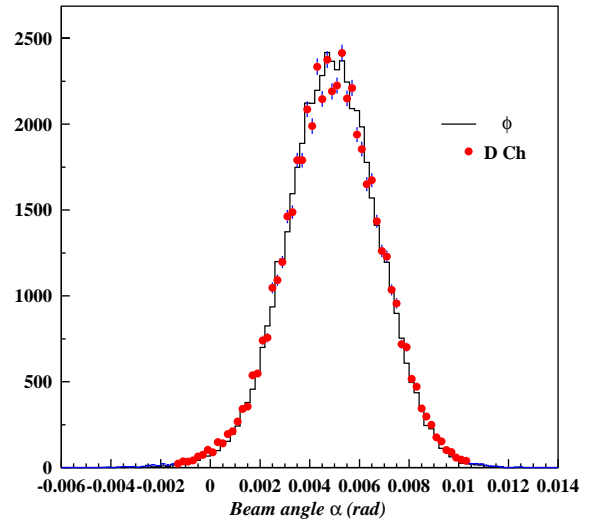


Fig. 15. The measured horizontal angular beam profile. The histogram was obtained using a combined fit to the hits in superlayers ϕ_1 and ϕ_2 . The dots were obtained using the delay chambers for the same events.

obtained using the delay chambers for the same events.

Fig. 17 shows the distribution of the difference in angle obtained with superlayer ϕ_1 , with respect to the value measured using the delay chambers. A

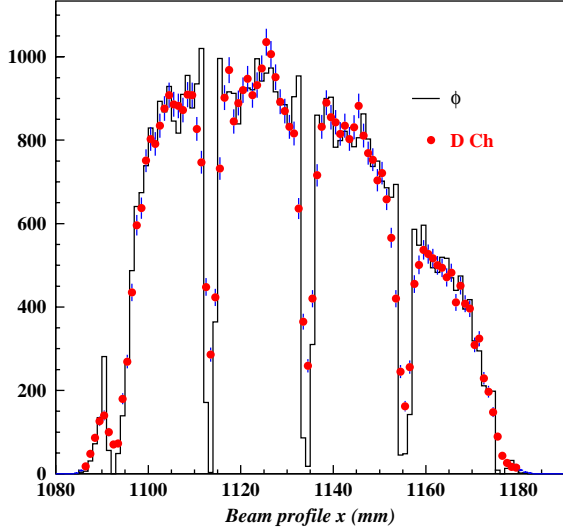


Fig. 16. The measured horizontal position beam profile.

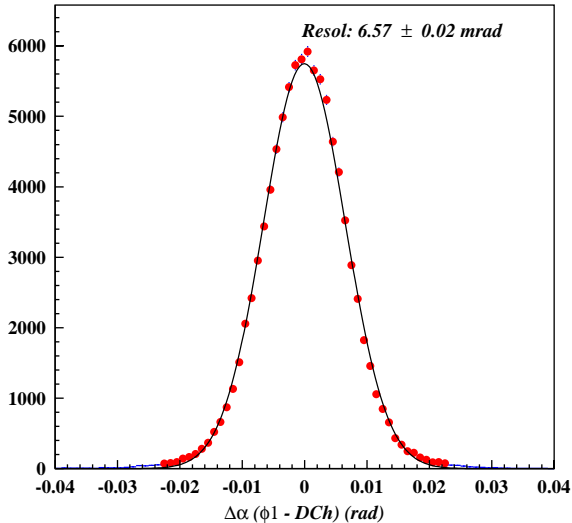


Fig. 17. Distribution of the difference in angle obtained with superlayer ϕ_1 , with respect to the value measured using the delay chambers (Run 624).

single superlayer angular resolution of 6.57 ± 0.02 mrad is obtained. For a hit position resolution of $180 \mu\text{m}$, a resolution of 6.20 mrad is expected.

Figs. 18 and 19 show the distributions of the difference in angle and position, respectively, measured using a combined fit to the hits in

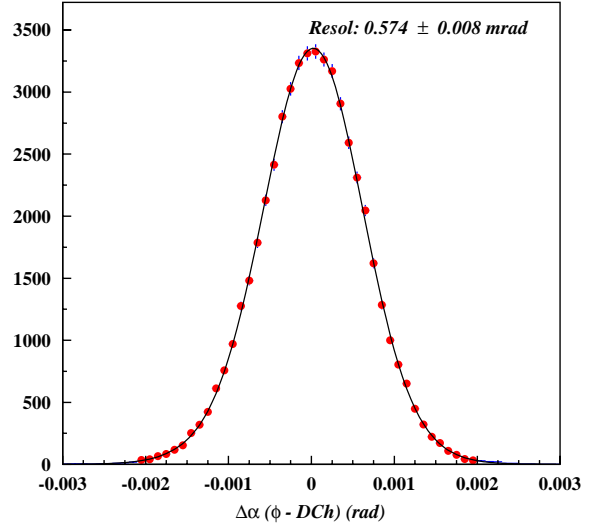


Fig. 18. Distribution of the difference in angle measured using a combined fit to the hits in superlayers ϕ_1 and ϕ_2 , with respect to the values measured using the delay chambers (Run 624).

superlayers ϕ_1 and ϕ_2 , with respect to the values measured using the delay chambers. A position resolution of 0.976 ± 0.007 mm (dominated by the error on the delay chamber extrapolation, as explained above), and a combined angular resolution of 0.574 ± 0.008 mrad are obtained. For a hit position resolution of $180 \mu\text{m}$, a position resolution of $64 \mu\text{m}$, and an angular resolution of 0.53 mrad are expected.

5. Test beam results

In this section we investigate the evolution of the chamber performance parameters, when the operating conditions are changed.

5.1. High-voltage scan

We studied the dependence of the drift velocity, resolution, and efficiency as a function of the wire and cathode voltages. In the first case, for constant $V_{\text{strip}} = 1800$ V and $V_{\text{cath}} = -1200$ V, the wire voltage was changed in the range 3400 – 3625 V at two different chamber positions.

The gas gain depends essentially on the amplification voltage, defined as the difference between

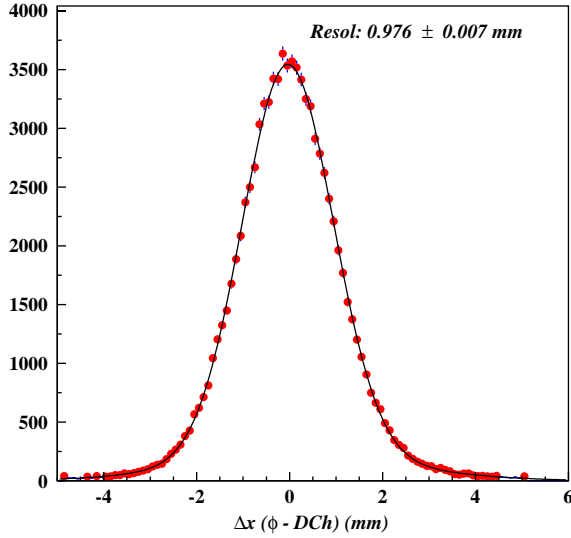


Fig. 19. Distribution of the difference in position measured using a combined fit to the hits in superlayers ϕ_1 and ϕ_2 , with respect to the values measured using the delay chambers (Run 624).

the wire and strip voltages. For constant V_{strip} , a change in V_{wire} in the previous range corresponds to a change in the amplification voltage in the 1600–1825 V range. The procedure described above was used to calibrate the runs with different values of V_{wire} . As explained in Section 4.1, once the T_0 is defined for each run from the derivative of the time box distribution (Gaussian mean value minus 5 ns), the drift velocity can be estimated from the meantime distributions. Table 4 displays the measured drift velocities as a function of the wire voltage. Within errors the drift velocity is constant and close to the 55 $\mu\text{m}/\text{ns}$ value that we use later as a fixed value to recalculate the T_0 's and to measure the rest of the chamber parameters.

Previous analyses [1,4] reported observations of a drift velocity dependence at a few percent level with the amplification voltage. This discrepancy can be understood by considering the correlation between T_0 and drift velocity, and the variation with the amplification voltage of the time resolution which affects significantly the T_0 definition when using alternative approaches (for instance through the changing width of the time derivative distribution: the sigma of this distribution turns

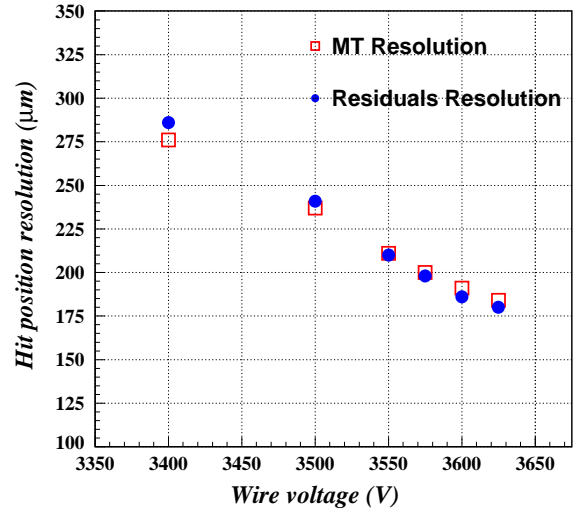


Fig. 20. Hit position resolutions (averaged over the three superlayers and over two positions in the chamber) as a function of the wire voltage.

out to vary from 5.3 ns at $V_{\text{wire}} = 3500$ V to 2.7 ns at $V_{\text{wire}} = 3625$ V).

Fig. 20 shows the hit position resolution as a function of V_{wire} , for segments with 4 hits and $\chi^2 < 0.3 \text{ mm}^2$, and both using the MT and Residual computation methods. Fig. 21 shows the measured efficiencies as a function of V_{wire} . A summary of all measurements can be found in Table 4. For a wire voltage value of 3550 V the resolution is still better than 220 μm and the efficiency 99.85%.

The cathode voltage was changed in order to test the parameter dependence on the drift voltage, defined as the difference between the strip and cathode voltages. The drift voltage value is responsible for the electric field values along the cell. In this test, cathode voltages in the range 1200–1400 V were studied, corresponding to drift voltage values between 3000 and 3200 V. For electric fields in this region, the drift velocity is expected to be saturated. No significant dependence of any chamber performance parameter on V_{cath} has been observed in this analysis.

5.2. Threshold-level scan

Analogously to the previous subsection, the dependence of the chamber performance

parameters on the discriminator threshold level was investigated. The threshold levels were changed in the range 10–30 mV, equivalent to 3–9 fC of integrated charge.

Fig. 22 shows the global T_0 shift dependence on the threshold level. The shifts are defined with respect to the 10 mV threshold T_0 value. From a linear fit, a slope of 0.146 ± 0.001 ns/mV is measured. Correspondingly, the apparent drift velocity at fixed T_0 decreases with the threshold (Fig. 23). Error bars on the drift velocities are dominated by the systematics related to a change of ± 1 ns in the T_0 subtraction.

Fig. 24 shows the hit position resolution dependence on the threshold value, measured with 4-hit segments having $\chi^2 < 0.3$ mm². Also, in

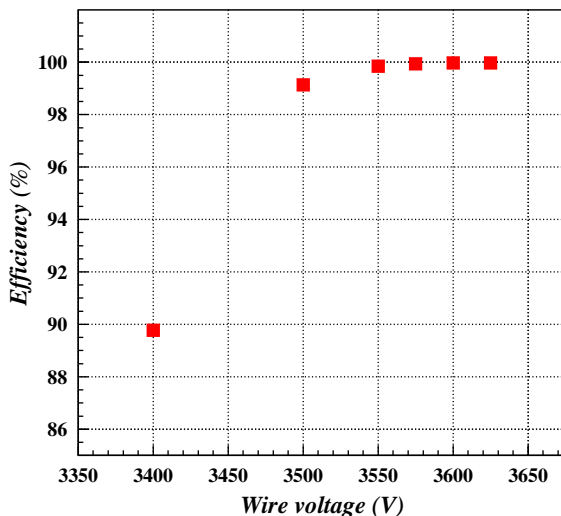


Fig. 21. Hit efficiency dependence on the wire voltage.

Fig. 25, the cell efficiency dependence on the threshold level (squares) is summarized. Both the hit resolution and the cell efficiency deteriorate as the threshold grows, as expected. Even for a threshold value of 30 mV (9 fC) the resolution is below 220 μ m and the efficiency larger than 99.85%.

6. Noise effects

In this section we investigate the behavior of the chamber performance parameters in the presence

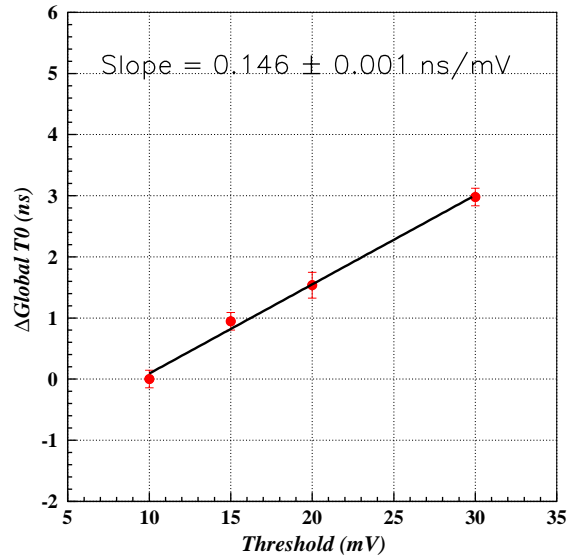


Fig. 22. Global T_0 shift dependence on the threshold level. The shifts are defined with respect to the 10 mV threshold T_0 value.

Table 4

Summary of the measured drift velocities (μ m/ns), hit position resolutions (μ m) and cell efficiencies (%), as a function of the wire voltage

Wire voltage (V)	3400	3500	3550	3600	3625
Drift velocity	54.9 ± 0.7	55.1 ± 0.3	55.1 ± 0.3	55.1 ± 0.3	55.1 ± 0.3
Resolution (MT)	276 ± 2	237 ± 1	211 ± 1	191 ± 1	184 ± 1
Resolution (Res.)	286 ± 1	241 ± 1	210 ± 1	186 ± 1	180 ± 1
Efficiency	89.77	99.13	99.85	99.97	99.97

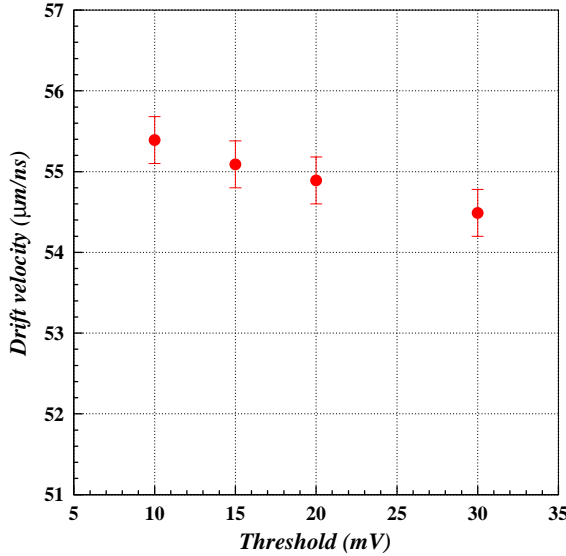


Fig. 23. Corresponding drift velocity dependence on the threshold level. Error bars on the drift velocities are dominated by the systematic related to a change of ± 1 ns in the T_0 subtraction.

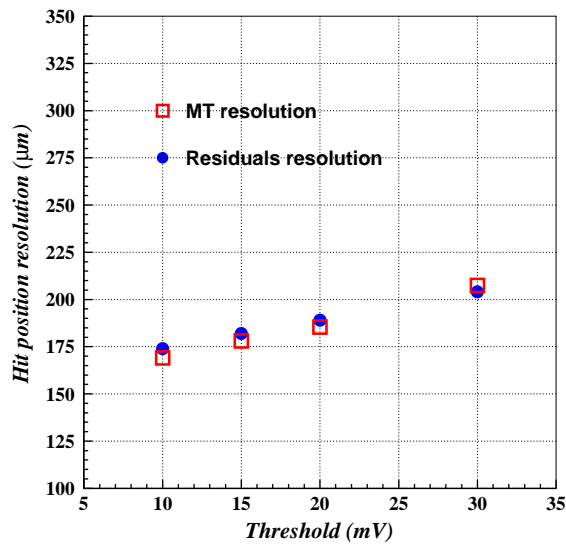


Fig. 24. Hit position resolution dependence on the threshold value.

of several levels of noise, corresponding to different filters of the gamma source. The noise signals are produced by photon conversion at the

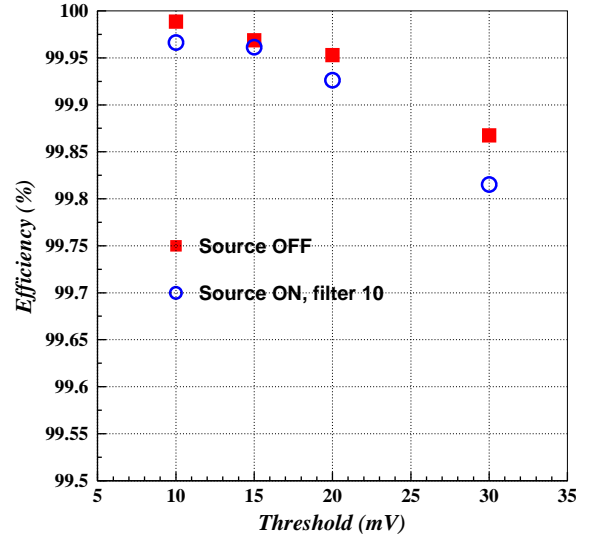


Fig. 25. Cell efficiency dependence on the threshold level, for two conditions of gamma irradiation: source off (squares) and filter 10 (circles).

chamber walls, and further ionization of the cell gas by the e^+e^- tracks.

6.1. Noise occupancy levels

We first compute the noise occupancy normalization, measured in noise runs. Events in noise runs are selected with random triggers in anti-coincidence with the “SPILL ON” signal. Figs. 26 and 27 show the noise occupancies as a function of the cell number for the three superlayers. Fig. 26 was obtained with the gamma source off. Fig. 27 is for gamma irradiation corresponding to a filter of 10. Fig. 28 shows the noise cell occupancy, averaged over all the cells in a given superlayer, for the three superlayers, as a function of the source filter value (F). The measured points are expected to be given by the formula

$$R(F) = R_1 \exp(-k \log(F)) + R_0 \quad (1)$$

where R_0 represents the intrinsic noise rate. The parameter k (if different from 1) translates from the nominal filter value to the actual one. Defining $\mathcal{F} = 10^k$, this number gives the actual reduction filter when a nominal filter of 10 has been applied. The parameter R_1 represents the noise level

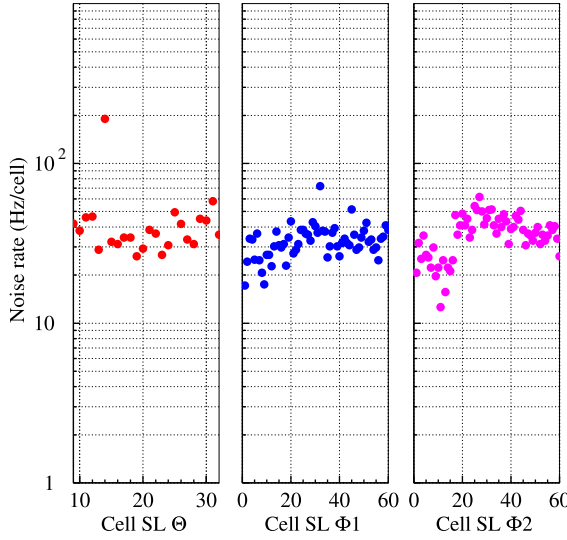


Fig. 26. The noise cell occupancy as a function of the cell number, for the three superlayers, and for gamma source off.

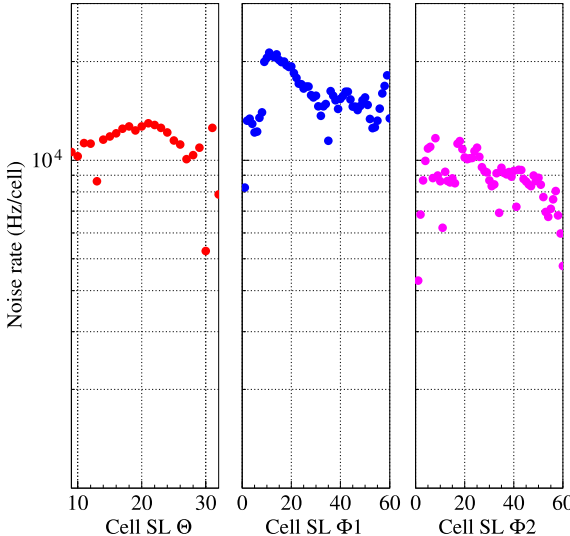


Fig. 27. The noise cell occupancy as a function of the cell number, for the three superlayers, and for gamma irradiation corresponding to a filter of 10.

without filter ($F = 1$). The fits are superimposed in Fig. 28, the parameters are given in Table 5.

The parameters R_0 and k (thus \mathcal{F}) appear to be superlayer-independent as expected. Calculating the corresponding averages over the three super-

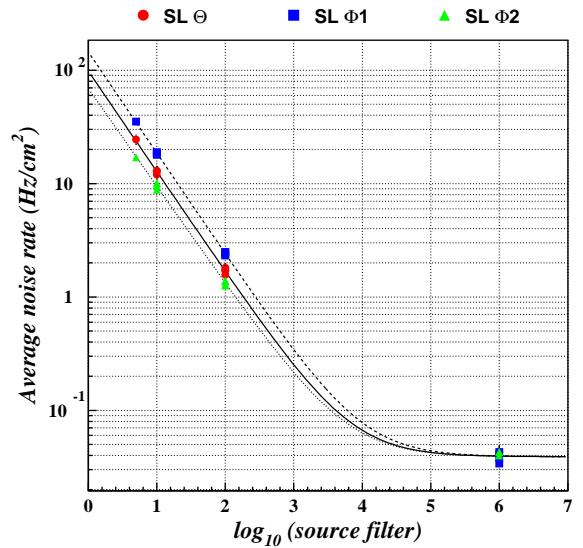


Fig. 28. The noise cell occupancy, averaged over all the cells in a given superlayer, for the three superlayers, as a function of the source filter value. The fits are discussed in the text.

Table 5

Parameters of the fit to the noise occupancy as a function of the source filter value, for the three superlayers. The meaning of the parameters is explained in the text

	SL θ	SL ϕ_1	SL ϕ_2
R_0 (Hz)	42 ± 3	37 ± 2	42 ± 2
R_1 (Hz/cm ²)	99 ± 13	145 ± 13	69 ± 5
k	0.89 ± 0.04	0.89 ± 0.03	0.86 ± 0.02
\mathcal{F}	7.7 ± 0.7	7.8 ± 0.4	7.3 ± 0.4

layers gives

$$R_0 = 40 \pm 1 \text{ Hz}, \quad k = 0.88 \pm 0.02, \quad \mathcal{F} = 7.5 \pm 0.3.$$

Note that the results on chamber performance discussed in the previous sections were obtained in the presence of a noise level given by R_0 . The hit background level, in the cells hit by the beam, is of order 10^{-4} , and therefore negligible. Indeed this noise was hidden below other small beam-related backgrounds in normal physics runs.

The values of the R_1 noise as a function of the superlayer change as expected, given their position and relative shadowing, in the face of the gamma source. The noise levels during LHC operation (originated on neutron capture) correspond to

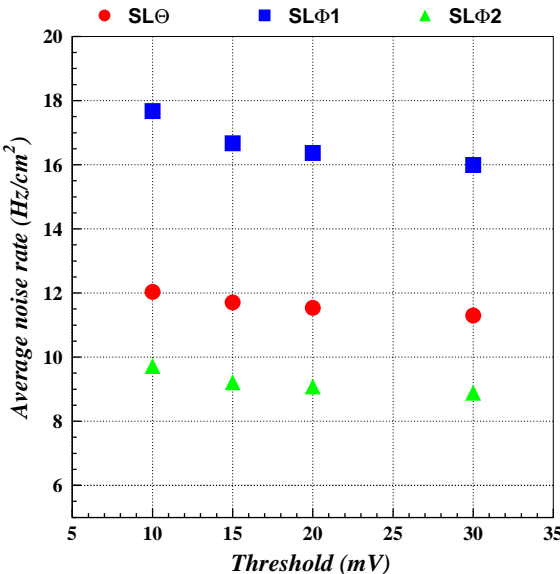


Fig. 29. The average noise cell occupancy dependence on the threshold value, for the three superlayers, and for gamma irradiation corresponding to a filter of 10.

nominal filters in the approximate range $F = 20\text{--}300$ (10–125) in superlayer ϕ_1 (resp., in superlayer ϕ_2). For the smallest absorption filter value studied here ($F = 5$), the noise level is 3.5 (1.7) times larger than the maximum one expected at LHC in any barrel muon chamber.

Fig. 29 shows the dependence of the noise level on the discriminator threshold, for a source filter of 10. The dependence is rather mild, as the noise hits are originated by charged track ionization. Even with a threshold of 30 mV, the noise rate is only reduced to $\sim 90\%$. On the other hand, the e^+e^- pair is quickly absorbed, and noise hits in different layers are expected to be rather uncorrelated. The noise is not assumed to generate by itself fake muons. To quantify this, we fitted segments in a pure noise run (Run 650, filter 10). In 70,000 events only one 4-hit segment resembling a muon was found.

6.2. Chamber performance in the presence of noise

In this subsection the influence of noise at the muon level is measured. In particular two topics should be clarified. First, how the noise disturbs

the identity and relative frequency of the fit segments. Second, how much the chamber performance parameters change in the presence of noise.

In order to do this, we started by modifying the fit algorithm. In the previous sections, a fit algorithm designed to maximize the efficiency in the absence of noise has been used. This fit algorithm was adequate in the idealized conditions of a test beam environment. However, in the presence of noise, pure hit efficiency is not always desired, as it might mean the inclusion of noise hits, and degradation of the fit segments.

The fit algorithm required in this section is more like the one that will be used at LHC, where often one will prefer a good fit with 3 hits from a bad 4-hit fit. We implement this condition by considering hits in the time window $0 < T_{\text{hit}} < 400$ ns, and requiring (conservatively) $\chi^2 < 1 \text{ mm}^2$.

If the χ^2 of a 4-hit segment is larger than 1 mm^2 it is assumed that the fit is picking a bad hit, thus degrading the quality of the fit. The bad hit is identified by studying the meantime correlation MT1 versus MT2. The bad hit is then removed and a 3-hit fit is tried. Finally, if the χ^2 of the 3-hit segment is smaller than 1 mm^2 the fit is kept, otherwise the fit is rejected. In case of several fits, the one with the largest number of hits, and then the one with the best χ^2 is considered.

We note that, with the new algorithm, the majority of old 4-hit segments with $\chi^2 > 1 \text{ mm}^2$ ("delta-rays") are transformed in good 3-hit segments (with the associated improved precision in the measured position and angle). The old segments with 3 hits and $\chi^2 > 1 \text{ mm}^2$ are just a few (1.4%) and low-quality, as shown in Fig. 12. Cutting them just adds to the geometric I-beam cell inefficiency.

We now verify that with the use of this simple new algorithm, the muon detection procedure is very insensitive to the noise, up to the smallest measured filter of 5.

We proceed by selecting events with a good segment ($\chi^2 < 1 \text{ mm}^2$) in superlayer ϕ_2 and we study superlayer ϕ_1 . As measured in the previous subsection, the effect of noise in superlayer ϕ_2 is a factor of 2 smaller than in superlayer ϕ_1 .

There are several situations that can be considered to happen in the presence of noise hits:

- (1) A 3-hit segment incorporates a noise hit and is promoted to 4-hit. This would change the relative fractions of events with 4-hit and 3-hit segments.
- (2) One hit in a 4-hit segment is masked by a noise hit, the remaining segment is degraded to 3-hit. Again, this would change the relative fractions of events with 4-hit and 3-hit segments, but in the opposite direction.
- (3) Several hits from a good segment associate with a noise hit to give a second lower quality fit. This would change the fraction of events with a second fit.
- (4) The fraction of events without a fitted segment changes.

We have studied these four possibilities, using the data. However as it turns out that all effects are very small, only the effects involving 4-hit segments are visible. The ones involving 3-hit or no fit events are negligible as they are proportional, in addition, to their small fractions ($\sim 12\%$ and $\sim 4\%$, respectively).

To disentangle effects #1 and #2 we have applied the following method: we simulate a filter-10 physics sample, by mixing the events of Run 624 (source off) with the events of noise of Run 650 (filter 10). In this case, only effect #1 is relevant. The fraction of events with 4-hit segments over the sum of events with 3-hit and 4-hit segments both in the original and modified Run 624 is $87.7\% \pm 0.2\%$. Effect #1 is thus confirmed to be negligible.

Effects #2, #3, and #4 were studied using the data. Runs with different levels of gamma irradiation (source off; filter 100, 50, 10, and 5) were analyzed, and the results compared. In all these runs, the chamber was operated at nominal conditions except for filter 5. Typical wire currents in superlayer ϕ_1 for filter 10 were $\sim 6 \mu\text{A}$ at nominal voltages. In the run with filter 5, V_{wire} was reduced to 3570 V in superlayer ϕ_1 in order to maintain currents below the $10 \mu\text{A}$ limit. The other two superlayers were operated at nominal conditions. No effect of this reduced voltage on the results below is expected, and none has been

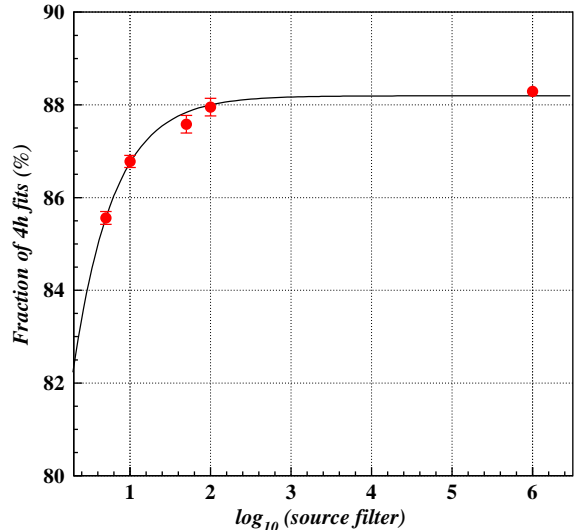


Fig. 30. The fraction of events with at least one segment in superlayer ϕ_1 , where the best segment is 4-hit, as a function of the filter value. The fit is discussed in the text.

observed, with the exception of the hit position resolution. This case is discussed later explicitly.

Fig. 30 shows the fraction of events with at least one segment in superlayer ϕ_1 , where the best segment is 4-hit, as a function of the filter value. The data points are well reproduced by a fit to Eq. (1), where the parameter k has been fixed to its known value of 0.88. The evolution of the data points is interpreted as caused by effect #2. Note that the size of the effect agrees very well with the result of a simple-minded calculation. Most important is that, even for a filter value of 5, the size of the effect is very small. For a filter value of 5, the fractions change by only 2.7%.

To test effect #3 we have studied the evolution of the fraction of events where a second segment in superlayer ϕ_1 has been reconstructed, as a function of the filter value. In Fig. 31 the case where the best segment in superlayer ϕ_1 has 4 hits is illustrated. Again the data points are well reproduced by a fit to Eq. (1), where the parameter k has been fixed to its known value of 0.88. This time however, the offset value (measured when the source was off) is dominated by events with two beam muons. Only the differences with respect to the offset are meaningful. For a filter value of 5,

the fraction of extra events with a second fit increases by only 1.2%. In the case where the best segment in superlayer ϕ_1 has 3 hits we observe no statistically significant variation.

Table 6 summarizes the measured numbers for all the fractions discussed in this subsection, corresponding to the five gamma irradiation levels studied in the present analysis.

Finally, the evolution of the chamber performance parameters (hit position resolution and cell efficiency) in superlayer ϕ_1 , as a function of the filter value, is presented in Figs. 32 and 33, and in **Table 7**. To simplify the comparison, in Fig. 32, the resolution for filter 5 has been corrected from the measured value at $V_{\text{wire}} = 3570$ V, to the

corresponding resolution at nominal $V_{\text{wire}} = 3600$ V using the measured dependence on the wire voltage (Fig. 20). Also, to be consistent with the values of the previous sections, the efficiencies in Fig. 33 have been calculated using the old fitting algorithm. In both cases, no significant dependence on the gamma irradiation level is observed. Only for larger discriminator threshold levels (30 mV in Fig. 25) a small dependence of the efficiency on the noise rate has been measured.

7. Interference with RPC

To test a possible disturbing influence of the RPC on the DT noise levels, the measurements

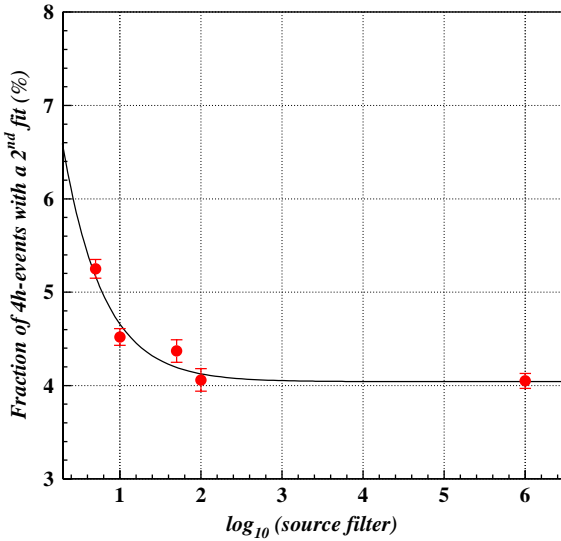


Fig. 31. The fraction of 4-hit ϕ_1 -segment events where a second segment in superlayer ϕ_1 has been reconstructed, as a function of the filter value. The fit is discussed in the text.

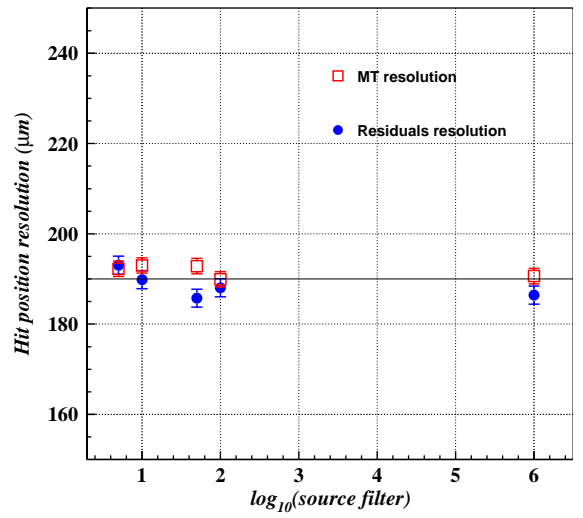


Fig. 32. The hit position resolution in superlayer ϕ_1 as a function of the filter value. The resolution for filter 5 has been corrected as explained in the text.

Table 6

The measured numbers (%) for all the fractions discussed in this subsection (see text), corresponding to the five gamma irradiation levels studied in the present analysis. All events must have a segment in superlayer ϕ_2

Filter value	No fit	4-h fit fraction	3-h fit fraction	4-h fit w/2nd fit	3-h fit w/2nd fit
Source off	3.6 ± 0.1	88.3 ± 0.1	11.7 ± 0.1	4.1 ± 0.1	5.2 ± 0.3
100	3.9 ± 0.1	88.0 ± 0.2	12.0 ± 0.2	4.1 ± 0.1	5.3 ± 0.4
50	3.4 ± 0.1	87.6 ± 0.2	12.4 ± 0.2	4.4 ± 0.1	5.8 ± 0.4
10	3.7 ± 0.1	86.8 ± 0.1	13.2 ± 0.1	4.5 ± 0.1	5.8 ± 0.3
5	3.6 ± 0.1	85.6 ± 0.1	14.4 ± 0.1	5.2 ± 0.1	5.8 ± 0.3

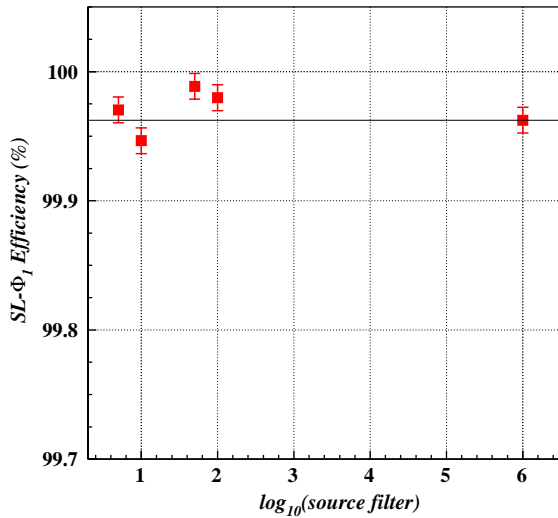


Fig. 33. The cell efficiency in superlayer ϕ_1 as a function of the filter value. Efficiencies have been calculated using the old fitting algorithm.

Table 7
The hit position resolution (μm) and cell efficiency (%) in superlayer ϕ_1 , as a function of the filter value

Filter value	Meantime resolution	Residuals resolution	Efficiency (old fit)
Source off	191 ± 2	186 ± 2	99.96 ± 0.01
100	190 ± 2	188 ± 2	99.98 ± 0.01
50	193 ± 2	186 ± 2	99.99 ± 0.01
10	193 ± 2	190 ± 2	99.95 ± 0.01
5	192 ± 2	193 ± 2	99.97 ± 0.01

All events must also have a segment in superlayer ϕ_2 . The resolution for filter 5 has been corrected as explained in the text. The efficiencies have been calculated using the old fitting algorithm.

discussed in the previous sections were analyzed for RPC HV on and off conditions. No difference has ever been observed. Even for the most sensitive sample (beam data when the DT HV was off) the size of the effect is consistent with zero. We conclude that the interference can be neglected.

8. Conclusions

Test beam results obtained at CERN Gif with the first produced CMS DT chamber have been presented. The chamber calibration and wire alignment procedure used in the data analysis has been described in detail using a typical run for illustration purposes. It has been shown that the performance of the chamber, coupled to an RPC, is satisfactory and fulfills all requirements. Results obtained from the comparison of the data taken in several operating conditions are in good agreement with test beam results for previous superlayer prototypes. No degradation of the chamber performance was found even with noise rates higher than the maximum one expected in any DT chamber during normal LHC operation.

Acknowledgements

We acknowledge the efforts of several technicians at CIEMAT who made possible the construction, test, transport and set up of the MB2 chamber. The collaboration of people from all labs involved in the CMS Muon Barrel Project, and from CERN, who participated in the test beam activities is also acknowledged.

References

- [1] CMS Collaboration, The muon project. Technical Design Report, CERN/LHCC/97-32, 1997.
- [2] F. Gasparini, et al., Nucl. Instr. and Meth. A 336 (1993) 91.
- [3] G. Barichello, et al., Nucl. Instr. and Meth. A 360 (1995) 507.
- [4] M. Aguilar-Benítez, et al., Nucl. Instr. and Meth. A 480 (2002) 658.
- [5] A. Colaleo, First results on RB2 muon barrel RPC detector for CMS, CMS Note CR-2002/009, 2002.
- [6] M. Cerrada, et al., Test beam analysis of the first CMS MB2 drift tube muon chamber, CMS Note 2003/007, 2003.
- [7] J. Christiansen, High performance time to digital converter, CERN/EP-MIC, 2002.